Gao et al. *Microsystems & Nanoengineering* (2026)12:174
https://doi.org/10.1038/s41378-026-01240-1

Microsystems & Nanoengineering
www.nature.com/micronano

ARTICLE Open Access

A novel bioinspired integrated system for simultaneous fog harvesting and energy supply

Hanpeng Gao[1], Li Li[1], Yamin Hu[1], Oliveira Henriques Moita Ana Sofia[2], Xi Wang[3], Zong Meng[1], Zhiwu Han[4] and Yan Liu[4,5]✉

Abstract

The escalating threats posed by global warming are intensifying freshwater and energy scarcity, driving the demand for integrated systems that harvest fog and supply power. However, existing systems are challenged because high-efficiency fog harvesters lack energy supply, whereas droplet-based generators have low water yield. Herein, we present a novel bioinspired integrated system that combines synergistic biomimetic dendritic structured surface with a droplet-based triboelectric nanogenerator for simultaneously harvest water and generate energy. Specifically, the synergistic biomimetic dendritic structured surface combines Laplace force, capillary force, and surface wetting gradient, enabling barrier-free droplet transport and highly efficient fog harvesting. Moreover, the optimized MXene-PDMS with Superhydrophobicity prevents water retention and deposit shielding on the triboelectric layer, enlarging the electrostatic area and enhancing charge output. Remarkably, the optimized SBDSS achieves a 9.7 g·cm^{-2}·h^{-1} fog harvesting rate, representing 125% and 430% of unprocessed and non-UV-irradiated surfaces, respectively. The integrated D-TENG provides a new approach for efficient harvesting energy from fog droplets in practical environments, with enhanced durability and stability. Intriguingly, the novel bioinspired integrated system supports the growth of barley (*Hordeum vulgare*), providing freshwater and LED lighting for plant growth. This system offers a viable solution to address water and energy challenges in agricultural systems.

Introduction

Global warming and persistent population growth have intensified freshwater and energy scarcity, especially in arid and semi-arid remote regions, where limited water availability due to long-distance transport challenges threatens hydropower generation, agricultural sustainability, and overall progress toward sustainable development[1–3]. Consequently, integrated water-energy systems that simultaneously harvest water and generate power from ambient sources offer a promising solution[4]. Conventional water harvesting methods such as desalination and groundwater purification have mitigated freshwater scarcity but at a high energy and environmental cost, worsening the global energy burden[5,6]. Emerging alternatives like fog collection offer a sustainable pathway to water security. Fog, a ubiquitous and renewable natural resource akin to sunlight and wind, remains largely untapped as a source of both water and energy[7,8]. If harnessed effectively, the energy within the system can drive the development of integrated water harvesting systems that are not limited by terrain, while also providing critical relief to remote, water-scarce regions that face both freshwater shortages and limited energy access, thereby contributing to sustainable development.

Fortunately, organisms in nature provide an inspirational source for fog harvesting systems[9]. For example, the Namib Desert beetle has significantly improved fog collection efficiency through special surface with wettability gradients and micro/nanostructures. The cactus spine exemplifies directional water transport through its conical geometry and surface-energy gradient, enabling continuous droplet movement toward the base, reducing coalescence time and enhancing fog collection efficiency[10]. Inspired by the Nepenthes alata peristome, a

---

Correspondence: Yan Liu (lyyw@jlu.edu.cn)
[1]Hebei Key Laboratory of Measurement Technology and Instrumentation, School of Electrical Engineering, Yanshan University, Qinhuangdao, P. R. China
[2]IN + - Center for Innovation, Technology and Policy Research, Instituto Superior Técnico, Universidade de Lisboa, Av. Rovisco Pais, Lisboa, Portugal
Full list of author information is available at the end of the article

biomimetic surface with sharp-edged microcavities suppresses droplet pinning, enabling highly efficient and continuous droplet transport[11]. The excellent fog-collecting surface mechanisms of these natural organisms have long been a hot topic in the scientific community. Driven by environmental concerns, this has led to the development of eco-friendly biomimetic fog harvesting systems with special wettability[12]. In our previous studies, a series of biomimetic metal surfaces with anisotropic wettability have been developed, which enable effective droplet manipulation and enhance fog harvesting rate[13,14]. However, these designs often suffer from single functionality without generating usable energy, and difficulty in integration, thereby undermining their practicality in real-world deployment.

Recently, advanced researches have reported the emergence of droplet-based triboelectric nanogenerator (D-TENG)[15–17]. which can convert the mechanical energy of falling water droplets into electricity, offering a promising pathway for harvesting energy from natural water sources such as rainfall and fog[18,19]. This technology presents a sustainable solution for powering miniaturized sensor in remote or off-grid environments. Although advanced progress has been made, current designs prioritize energy conversion over water production, resulting in generally inadequate water collection capacity that fails to meet the needs of regions with scarce energy and fresh water[17,20–22]. Furthermore, low material efficiency, poor durability, challenges in system integration, and the difficulty in balancing conductivity with triboelectric performance also limit their practical application. Therefore, a truly transformative solution must integrate efficient water collection with energy generation, the dual potential of fog as a combined water and energy resource.

In this work, we propose a novel bioinspired integrated system (NBIS) that combines synergistic biomimetic dendritic structured surface (SBDSS) for efficient fog harvesting with a droplet-based triboelectric nanogenerator (D-TENG) for energy supply. More specifically, inspired by the anisotropic wettability surface of the Namib Desert beetle, the curvature gradient of cactus spines, and the directional transport peristome surface of Nepenthes alata, we developed the SBDSS on the titanium (Ti) substrate to enhance fog collection efficiency via simple laser etching and UV irradiation-induced modification. The surface features interlaced wetting pattern to efficiently capture fog by promoting droplet growth and aggregation, and a wettability gradient (water contact angle from 87°to 0°) on the wedge-shaped microchannels to enhance the droplet motion. After analyzing the temporal evolution droplets on the microchannels, the effect of different structural parameters of SBDSS on the collection efficiency is investigated, further elucidating the mechanisms by which the curvature gradient, and wetting gradient, directional transport structure surface facilitate fog harvesting and droplet transportation. Furthermore, the energy of droplets during their fall is often overlooked. Here, the D-TENG is integrated to convert the kinetic energy of falling droplets into electricity, while achieving efficient water collection and droplet-based power generation. More importantly, the introduction of the MXene-PDMS achieves optimal superhydrophobicity (WCA 152°) and enhanced electrical output while effectively mitigating performance degradation caused by sediment shielding and surface wetting, converting the mechanical energy of falling droplets into electricity with excellent output performance while enhancing durability. Finally, by powering photosynthesis-enabling LED lighting through its generated current, the NBIS autonomously irrigated high-germination barley *(Hordeum vulgare*) seedlings while maintaining optimal water yield. This demonstrates the dual functionality of water and energy for off-grid agriculture. This integrated system advances low-carbon agriculture and synergizes water-energy-food nexus objectives.

Results and Discussion

Design and Concept of the System Integration

As a sustainable solution for global freshwater crises, bioinspired fog harvesting has attracted widespread attention. Nevertheless, conventional harvesters often suffer from significant inefficiency in synchronizing droplet capture with rapid transport. In addition to this hydraulic limitation, a critical opportunity is often overlooked: the mechanical energy in descending droplets, which could serve as a decentralized electrical source, remains largely untapped.

To address the above challenges, this work presents a novel bioinspired integrated system (NBIS), designed to alleviate water scarcity and produce clean energy, thereby enhancing its potential for practical deployment (Fig. 1a). As shown in Fig. 1a-II, the key feature of the synergistic biomimetic dendritic structured surface (SBDSS) is its functional integration of multiple biological design principles, combining the anisotropic wettability of the Namib Desert beetle, the curvature gradient of cactus spines, and the directional liquid transport characteristics of the peristome surface of *Nepenthes alata*. Preparing SBDSS involves structural designs incorporating coupled wettability/structural gradients achieved through laser ablation and reversible physical modification. Meanwhile, each dendritic structure serves as condensation sites. As fog condenses, nucleation preferentially occurs at the apexes of the wedge-shaped branches. The wedge-shaped trunk and tapered lateral branches collectively enable directional continuous fog water capture. To utilize the typically wasted energy from droplets, the system integrates the fog-collection capability of the SBDSS with a

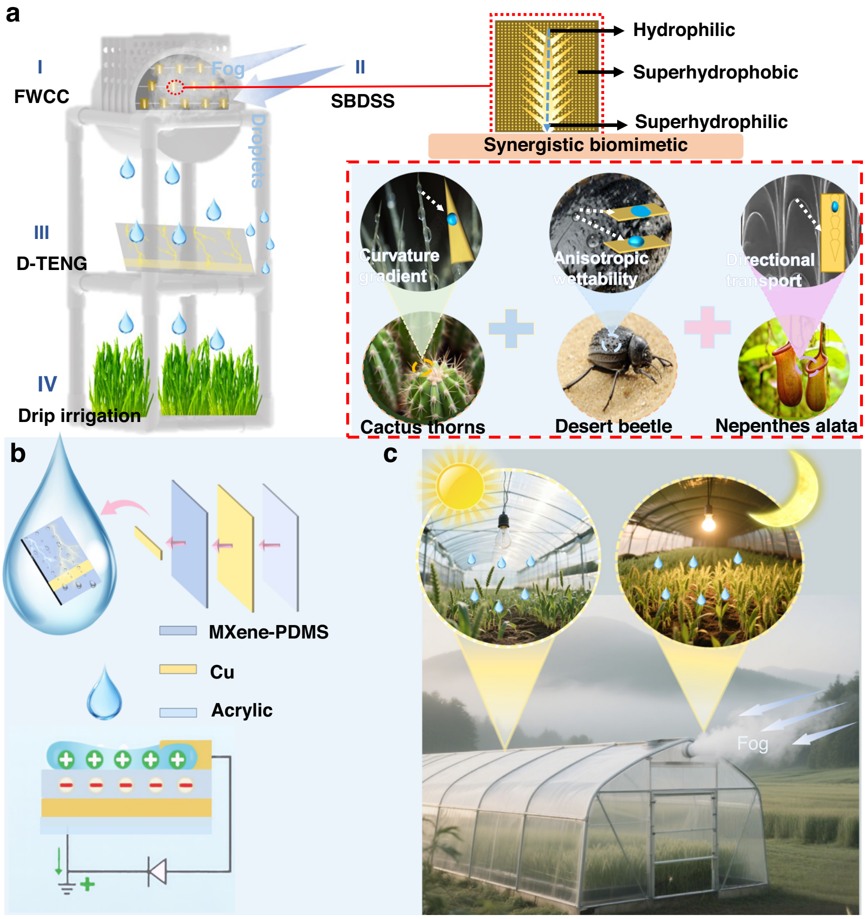

Fig. 1 System design and working principle. a Schematic illustration of a NBIS: (I) Modular device configuration comprising fog water converter container (FWCC); (II) SBDSS bioinspired fog-harvesting surface engineered through synergistic biomimetic of Cactus thorns, Namib desert beetle, and *Nepenthes alata* to enable efficient droplet capture, coalescence, and transport; (III) droplet-driven triboelectric nanogenerator (D-TENG); (IV) Harvested water is utilized for drip irrigation. **b** Working principle of the D-TENG, illustrating charge transfer at the solid–liquid interface. **c** Fog-harvesting and autonomous irrigation for off-grid micro-agriculture in arid regions

droplet-based triboelectric nanogenerator (D-TENG) is demonstrated by the system, which converts droplet mechanical energy into electrical power. As water accumulates, gravity drives droplets onto the D-TENG (Fig. 1a-III). Upon impacting the MXene-PDMS dielectric surface, droplets deform, redistributing surface charges. Contact with the top Cu electrode maximizes electrostatic-to-electrical conversion, spiking current voltage (Fig. 1b). Finally, the droplets slide off the D-TENG surface and fall onto plant roots, enabling off-grid irrigation solely powered by atmospheric water. This device constitutes an energy-supply integration platform for greenhouses, enabling fog capture, mechanical-to-electrical conversion (powering crop lighting), and irrigation (Fig. 1c).

By optimizing the multi-level functional architecture, the system achieves coordinated droplet capture, collection, and transport, ensuring stable operation of the droplet-based triboelectric nanogenerator (D-TENG). This study presents an integrated system design method grounded in "synergistic water-energy capture" that shifts the focus from single-function optimization and offers a sustainable solution for regions facing concurrent shortages of electricity and water resources.

Fabrication and characterization of SBDSS

In this study, titanium (Ti) sheets were selected as the substrate materials, motivated by their inherent excellent biocompatibility, corrosion resistance, and surface modifiability particularly in applications demanding controlled wettability, which are essential for constructing stable and functional biomimetic dendritic architectures. As depicted in Fig. 2a, to realize the interlaced wetting pattern on surfaces, a multi-step fabrication protocol was employed, integrating sequential laser processing, thermal treatment, and UV

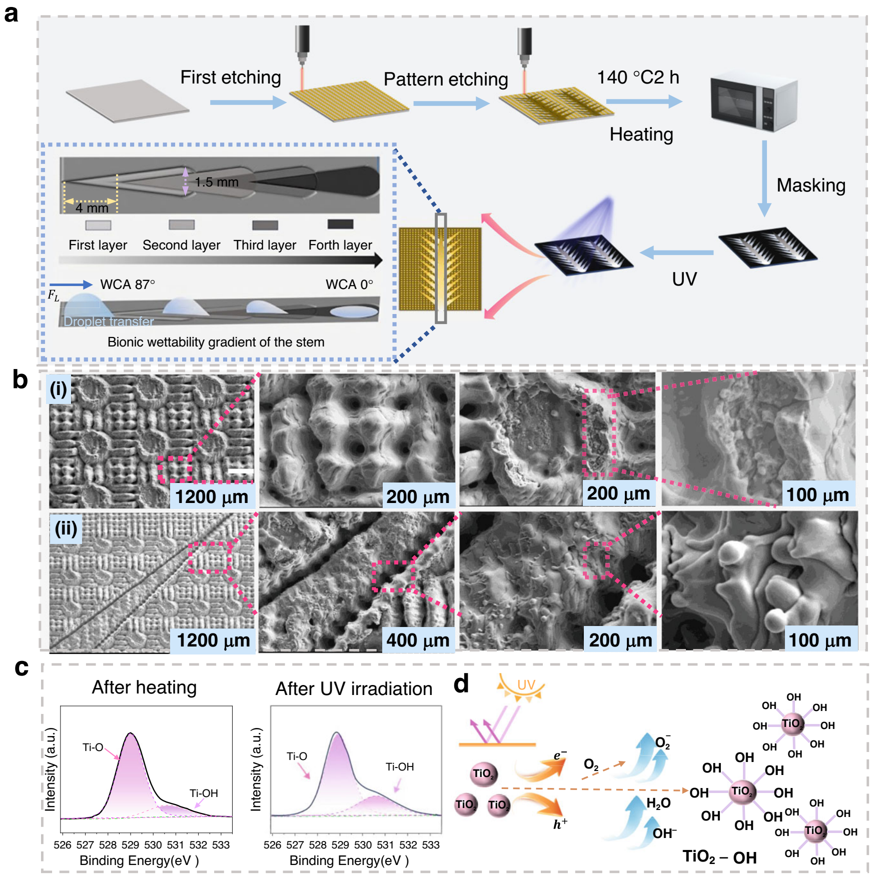

Fig. 2 Schematic of Fabrication process and UV exposure process. a Schematic of the fabrication process of the SBDSS structure **b** SEM images of the surface at different magnifications. Scale bars: 200 μm (top left), 100 μm (top right, bottom left), 50 μm (bottom right). **c** XPS spectra of O1s peaks under heating and UV irradiation conditions. **d** Schematic of the UV exposure process. UV light interacts with the TiO_2 surface, generating charge carriers that modify the surface chemistry

exposure[23,24]. These scalable patterning/texturing routes provide a practical pathway to translate the concept to large-area manufacturing (detailed in Supporting information, Note 2). Water contact angle (WCA) measurements in Fig. S1a indicate the initial surface state, characterized by a smooth topography, exhibited intrinsic hydrophilicity with a WCA of 74°. Upon controlled laser irradiation, rapid droplet spreading on the Ti surface (Fig. S1b), confirming its successful transition to a Superhydrophilic (SHL) state. Furthermore, after heating-induced treatment, the surface demonstrates a transformation to a superhydrophobic (SHB) state with low surface energy, with a measured WCA reaching 153° (Fig. S1c). The result shows that, high WCA signifies the establishment of a composite Cassie-Baxter wetting state, where air is effectively trapped within the surface microstructures[25,26]. A mask was then applied to the heated titanium substrate. With the aim of creating a wettability gradient, a color gradient was generated along the main trunk of the dendritic pattern by controlling the degree of UV exposure across different areas. The UV-exposed hydrophilic zones exhibited a continuous range of WCAs from 0°(fully irradiated, reverting to superhydrophilicity) to 87° (Fig. S2), thus finalizing the fabrication of the sample.

Laser etching was performed on the pristine Ti surface. Under laser ablation, the titanium surface melted and resolidified to form macroscopic periodic arrays (Fig. 2b-i). At the micro-nano scale, hierarchical structures nanoparticle clusters increased the surface roughness, thereby facilitating subsequent modification (Fig. 2b-ii). Fig. S3a shows the Ti substrate surface, while Fig. S3b and Fig. S3c display changes in the first to third layers of the patterned part, respectively. Fig. S3d highlights the branching morphology within the structure, and illustrates features outside the patterned region, providing a comprehensive view of the structural organization and its surrounding environment. Subsequent high-temperature heat treatment leveraged thermal stability of titanium to preserve the multi-scale micro-nano structure (macroscopic arrays and micron roughness). Elemental analysis of Ti surface detected carbon (C) and oxygen (O) in addition to titanium (Ti), further confirming the oxidation of the native Ti layer during laser etching (Fig. S4). X-ray photoelectron spectroscopy (XPS) was to probe the surface chemical composition and states of the samples. The survey spectrum (Fig. S5) distinctly shows characteristic peaks for O1s, Ti2p, and C1s, confirming the presence of oxygen, titanium, and carbon (the C1s signal is likely adventitious, originating from surface contaminants). High-resolution analysis of the Ti2p region reveals a spin-orbit doublet with the Ti $2p_{3}/_{2}$ and Ti $2p_{1}/_{2}$ peaks located at binding energies of 458.6 eV and 464.3 eV, respectively, indicative of a predominant Ti^{4+} oxidation state. To unravel the mechanism underlying the reversible wettability transition, the XPS test of the O 1 s peak spectrum was performed (Fig. 3c). The fitted spectrum discloses two distinct chemical environments for oxygen: lattice oxygen (O^{2-}) at 528.9 eV and surface hydroxyl groups (OH^{-}) at 530.6 eV. Notably, high-temperature treatment leads to a marked intensification of the Ti–O component. Conversely, subsequent UV illumination triggers the enhancement of the Ti–OH signal, accompanied by a concomitant decrease in the Ti–O peak intensity. Correlating these spectral changes with wettability measurements allows us to conclude that the dynamic equilibrium between hydroxyl and lattice oxygen populations is the primary driver of the wettability switch. A proposed mechanism for this interface wetting behavior is schematically illustrated in Fig. 3d. Thermal treatment promotes oxygen adsorption, facilitating the conversion of surface Ti–OH groups into Ti–O bonds, thereby inducing a transition to a hydrophobic state. Upon exposure to ultraviolet light ($\lambda \leq 387$ nm), the photoactive TiO_2 surface oxidizes adsorbed water molecules (H_2O) or hydroxide ions (OH^{-}), leading to the reformation of a dense, anchored layer of hydroxyl groups (–OH). This results in a hydroxylated TiO_2 surface (denoted as TiO_2–OH), characterized by uniform distribution of –OH groups on the nanoparticle surface, which confers hydrophilic character. The UV irradiation controlling wettability transition is quantitatively demonstrated in Fig. S6, which plots the WCA against reaction time at different positions on a gradient wedge after UV irradiation and gradient oxidation. The WCA transitions from 153° to values between 0° and 87°, confirming a switch from hydrophobic to hydrophilic behavior. This reversible transition is fundamentally governed by the competitive dissociative adsorption of H_2O and O_2 molecules at oxygen vacancy sites within the TiO_2 structure (detailed in Supporting information, Note 3).

Systematic characterization revealed the evolution of the microstructure and surface energy of the titanium plate under different modification treatments. Laser ablation created a hierarchical micro/nano-structure, and although subsequent heating induced nano-level sintering, the overall topology and function of the rough substrate remained intact. This structural stability enables dynamic switching of the interfacial wettability between hydrophilic and hydrophobic states through UV irradiation of masked areas. These findings provide key evidence for understanding the wettability transition mechanism and establish a theoretical foundation for future system optimization.

Dynamic wettability and theoretical analysis of water collection

Directed droplet motion on surfaces depends on wettability and structural gradients. The resulting surface tension imbalance between droplet front and rear sides creates a driving force for movement. Regions with varying wettability enable spontaneous droplet motion. Inspired by the conical structure of cactus thorns[27,28], a wedge-shaped groove is designed to guide droplets along specific paths (Fig. 3a). The wedge angle (α) creates a Laplace pressure gradient, driving top-to-bottom droplet movement[29]. This gradient is essential for spontaneous transport. The Laplace pressure difference across the droplet is affected by the local radii of curvature at the droplet-solid contact points. Following expansion-contraction cycles, droplets move within the groove under the Laplace pressure gradient ΔP, expressed as:

$$\Delta P = 2\gamma_{\mathrm{d}}\left(\frac{1}{R_1}-\frac{1}{R_2}\right)1$$

Here, R_1 (the front curvature radius) and R_2 (the rear curvature radius) represent the local radii of the three-phase contact line between the droplet and the solid surface. γ_{d} is the surface tension of the droplet. The self-driving force is equivalent to the Laplace pressure. The Laplace pressures acting on both ends of the droplet, directed inward, have different magnitudes, leading to a Laplace pressure difference. α (wedge angle) and h (groove height) are the two key parameters of the wedge-shaped groove. Therefore, parameter optimization was performed to enhance spontaneous droplet transport performance. As shown in Fig. 3b, the effect of varying wedge angles ($\alpha = 4°$, 6°, 8°, and 10°) on droplet transport velocity is demonstrated. The droplets move along a single-layer wedge-shaped structure with a length of 20 mm. At a wedge angle of 4°, a 4 μL droplet reaches the end in 0.2 s with a maximum velocity of 112.3 mm/s. The maximum deformation of the droplet does not significantly change with increasing volume, and the velocity variation across smaller droplet volumes remains minimal.

Nevertheless, the maximum velocity of droplets at different volumes was influenced by the wedge angle. As the wedge angle increases, the transport velocity of the droplet

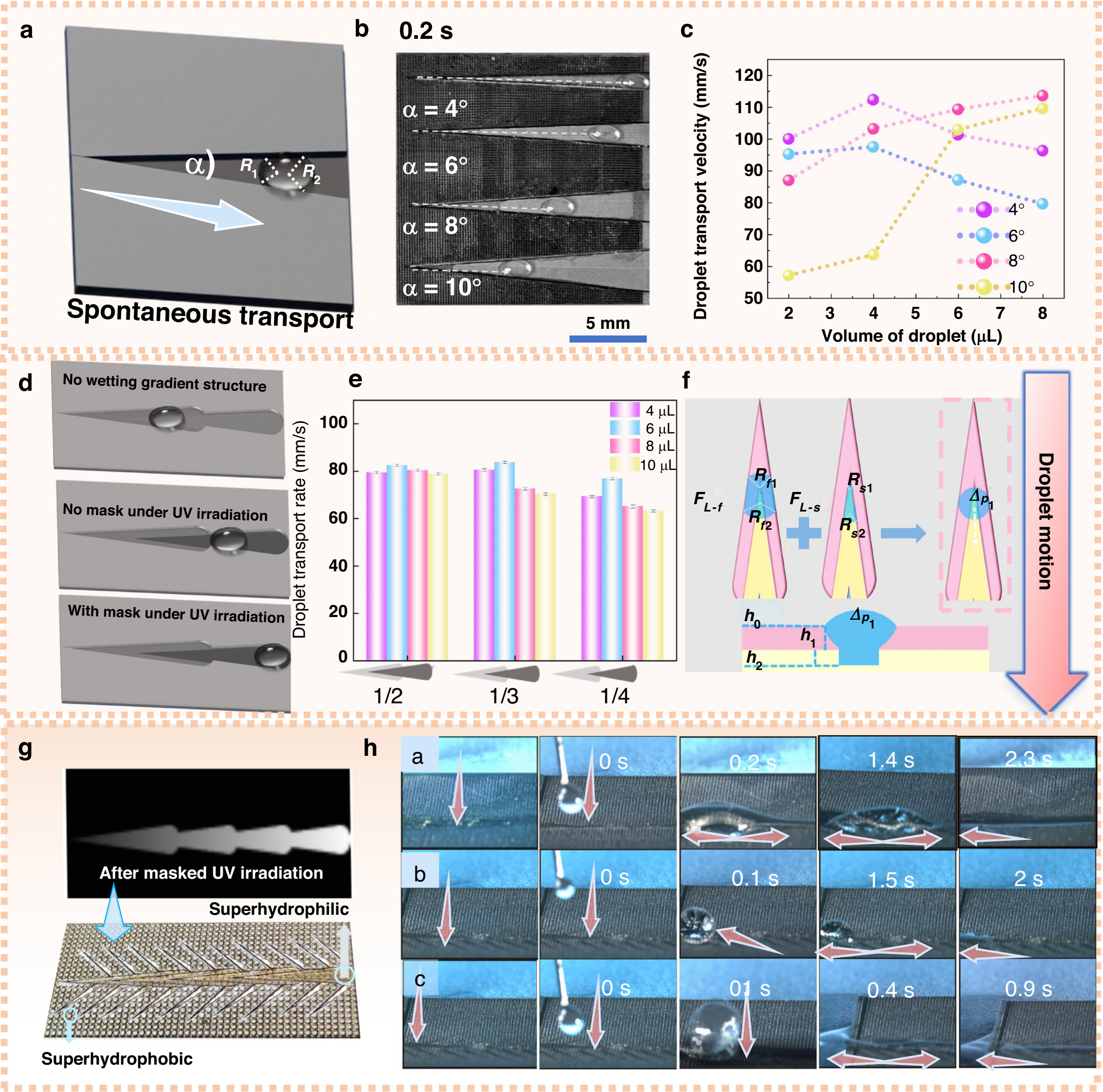

Fig. 3 Droplet transport and motion under varying surface conditions. **a** Schematic illustration of spontaneous droplet transport along a surface with wedge angles (α). **b** Snapshots showing spontaneous transport of a droplet over time (α = 4°, α = 6°, α = 8°, and α = 10°). **c** Droplet transport velocity as a function of droplet volume for different wedge angles (α). **d** Schematics demonstrating the experimental setups: (top) no wetting gradient structure, (middle) no mask under ultraviolet irradiation, and (bottom) with mask under ultraviolet irradiation. **e** Interlocking between internal/external wedge structures. **f** Illustration of droplet motion driven by Laplace forces. **g** Illustration of the SBDSS showing the wettability gradient within the gradient groove, transitioning from superhydrophobic to superhydrophilic. **h** (**a**–**c**) showing the motion of droplets on the SBDSS surface

increases as well. This can be attributed to the enhanced Laplace pressure gradient with increasing wedge angle. For example, at a wedge angle of 8°, an 8 μL droplet reaches a maximum velocity of 113.6 mm/s (Fig. 3c). The results confirm that the wedge angle plays a critical role in optimizing droplet transport efficiency, while the maximum deformation of the droplet remains relatively unaffected by changes in volume. According to the formula (Link to formula (1)), a smaller droplet radius of curvature results in a greater Laplace pressure. In the wedge-shaped groove, as the droplet moves farther from the apex, the local width increases, which causes a decrease in Laplace pressure. Additionally, as the wedge angle and groove length increase, the time required for the droplet to accumulate at the wide end also increases. This accumulation results in a droplet of specific height forming at the wider end of the groove. To enhance droplet transport on wedge-shaped hydrophilic patterns, inspired by the directional liquid-transporting lip of *Nepenthes alata*, which features periodic beak-like microcavities. This motivated the development of an asymmetric, droplet transport-separated, two-dimensional surface designed for unidirectional long-distance droplet transport[30]. Each wedge unit is connected by a hydrophilic arc, enabling rapid water storage. Furthermore, surface curvature facilitates droplet transport by enhancing mobility. The distribution of each unit on the track and the corresponding processing length is shown in Table S1. However, to achieve continuous spontaneous directional transport across a series of wedge-shaped grooves, droplets must primarily move along the longitudinal axis of groove, minimizing mass loss and maintains transport velocity. Inter-unit connections create energy barriers that disrupt motion. Variations in wedge angles cause droplets to lose contact with groove edges at distinct positions due to width disparities. Reducing these connection energy barriers promotes continuous transport. This study introduces structural and wettability gradients between adjacent groove units, providing driving forces for sustained droplet movement across connections. As illustrated in Fig. 3d, the droplet transport behavior is examined under different experimental conditions. In the first setup, where no wettability gradient structure is present, the droplet is guided along a simple wedge-shaped groove. The absence of a wettability gradient results in a relatively slow movement, with the droplet reaching the end of the groove at a velocity of only 30.9 mm·s^{-1}, which is insufficient to enable effective inter-node transport. In the second setup, when UV irradiation is applied without any wettability gradient structure, the droplet movement is slightly influenced, but no significant enhancement in velocity is observed. The surface modifications induced by UV light, without the aid of a mask to guide the wettability pattern, do not lead to any substantial improvement in droplet transport. In contrast, the third setup, where a mask is used under UV irradiation to create a controlled wettability gradient, shows a marked improvement in droplet velocity. The wettability gradient, which is introduced by the mask, enhances the movement of the droplet by creating differential interaction regions, thereby increasing the Laplace pressure along the groove. This combination of structural and wettability gradients significantly boosts the droplet transport speed. These results highlight the crucial role of wettability gradient structures in optimizing droplet transport, with the use of a mask under UV irradiation proving to be an effective method to improve droplet velocity. With wettability gradients, droplets are co-driven by the internal wedge, structural gradients, and wettability gradients during node transit. At a total wedge depth of 100 μm (Fig. S7a), the droplet achieves significantly enhanced velocity at nodes. This analysis reveals that the primary resistance originates at nodes, where droplets must elevate their center of mass to traverse the junction. Additionally, node cross-sectional constriction induces counteracting Laplace pressure. When node depth is fixed, the reverse Laplace pressure at nodes can be modulated by adjusting node length. Under varying node lengths, the internal-wedge terminal velocity of droplet exhibits a non-monotonic trend, peaking at 1.5 mm where sustained high mobility is maintained (Fig. S7b). Optimal parameters for multilevel biomimetic structures require droplet volume compatibility. The color gradient represents variations in threshold volume for different combinations of wedge angle and track width. Larger wedge angles and wider track widths correlate with higher threshold volumes, and this information is essential for optimizing design configurations to enhance fluid transport efficiency. Based on the optimal track depth of 100 μm, Fig. S8 presents the heatmap showing the relationship between Wedge Angle (α), Track Width (w), and Threshold Volume (μL). The color gradient represents variations in threshold volume for different combinations of wedge angle and track width. Larger wedge angles and wider track widths correlate with higher threshold volumes, providing insight into the geometric influence on droplet transport. To achieve volume matching, interlocking between internal/external wedge structures was optimized, evaluating three distinct assembly designs (Fig. 3e). Droplet movement on multistage wedge-interlocked platforms follows two distinct mechanical stages. Prior to reaching node regions, Laplace pressures and forces acting at droplet ends—directed toward its interior—differ in magnitude.

As shown in Fig. 3f, the droplet dynamics within wedge-shaped grooves are demonstrated, where two key Laplace forces govern the motion. The first-stage Laplace force, denoted as F_{L-f}, originates from the interaction between the droplet and the internal wedge structure, initiating the droplet's movement. The second-stage Laplace force, F_{L-s}, arises from the external wedge structure and further accelerates the droplet. The combined effect of these forces generates a coupled driving force, ΔP_1, which induces deformation of the droplet's surface and facilitates self-propulsion through the gradient-structured channel, expressed as:

$$F_{\mathrm{L-f}} = 2 \cdot \gamma_d \cdot \left(1/_{R_{f1}} - 1/_{R_{f2}}\right) \tag{2}$$

$$F_{\mathrm{L-s}} = 2 \cdot \gamma_d \cdot \left(1/_{R_{\mathrm{s}1}} - 1/_{R_{s2}}\right) \tag{3}$$

$$\begin{aligned}\mathrm{P}_1 = {} & \int_{h_0}^{h_1} \left(F_{\mathrm{L}-f} \cdot S_f/V + F_{L-s} \cdot S_s/V\right) dh \\ & + \int_{h_1}^{h_2} F_{\mathrm{L}-s} \cdot S_s/V dh\end{aligned} \tag{4}$$

The magnitude of these forces is influenced by several key parameters: the curvature radii of the droplet at the front R_{f_1} and rear R_{f_2} ends, and the curvatures of the solid surfaces at the droplet's contact points R_{s_1} and R_{s_2}. Additionally, the contact area between the droplet and the surface (S), as well as the droplet volume (V), play crucial roles in the dynamics of the system. As the droplet traverses the node, it experiences a reverse Laplace force from the external wedge structure, while the internal wedge structure applies tensile stress. Although the external wedge continues to apply forward driving force, the droplet simultaneously encounters resistance Fv at the internal wedge end. This resistance comprises pinning forces and friction arising from contact-line interactions (e.g., contaminants or molecular adhesion), collectively impeding motion. While wedge-shaped gradient channels enhance transport efficiency, pinning and friction at node boundaries hinder the process. To mitigate this, a wettability-gradient strategy interconnecting the wedge channels is proposed, minimizing transport resistance. (Fig. S9). In this configuration, droplet motion toward the ridge base is governed by the vector sum of Laplace forces, capillary forces, adhesive forces, and gravitational components, as defined below:

$$F = \Delta \mathrm{P}_1 + F_{cap} + G - Fv \tag{5}$$

Capillary force F_{cap} induced by multiscale rough microstructures in groove channels is the primary driving mechanism. Wedge-shaped grooves establish wettability gradients that generate surface tension variations along their length. Under wettability gradients, contact angle variation creates position-dependent capillary forces. By implementing gradient masks with UV modification within wedge structures, linear wettability gradients along the wedge axis are achieved. Capillary force at any position is thus described as:

$$F_{\mathrm{cap}}(x) = \gamma \cdot L(x) \cdot \cos(\theta(x)) \tag{6}$$

Here, $\theta(x)$ denotes the contact angle, governed by the surface wettability gradient. The contact angle transitions from 87° to near 0° along a hydrophilic gradient, progressively increasing the capillary force. This enhanced force reduces pinning and friction at the contact line within an unoptimized channel, facilitating more efficient droplet transport and improving water collection efficiency. A gradient hydrophilic dendritic micropattern was fabricated on a superhydrophobic substrate (Fig. 3g). A 2 μL droplet deposited onto horizontally oriented dendritic wedge branches underwent rapid short-range directional transport driven by Laplace pressure, spreading across the entire hydrophilic-patterned surface with 0.42 s (Fig. S10). To investigate dendritic structure and wettability gradient effects, droplets were released from 1 cm height onto different regions. Due to synergistic structural/wettability gradients (Fig. 3h-a), droplets impacting the midpoint of the main trunk spread rapidly upon impact. Lateral wettability gradient induced bidirectional elongation along the gradient direction. Interfacial energy gradients created asymmetric contact angles: smaller angles at the hydrophilic left (promoting spreading) and larger angles at the hydrophobic right (causing contraction). Capillary forces within the gradient structure eventually stabilized the droplet into uniform distribution. In Fig. 3h-b, the leading edge of the droplet contacted the superhydrophobic surface while its trailing edge touched a superhydrophilic wedge branch, unidirectional migration toward the main trunk occurred under gradient-driven forces. As surface energy equilibrated, localized recoil transformed the droplet from spherical to a smaller satellite droplet. In Fig. 3h-c, impact at the superhydrophilic terminus of the main trunk caused rapid deformation and groove-gradient migration. The droplet transitioned from bulk liquid to thin film, enabling extended spreading and enhancing fog collection refresh rates. Based on a theoretical analysis of water transport on the surface, four identical 8° wedge-shaped channels with wettability and structural gradients were designed. These channels are interconnected dendritically through central interlocking and side branches and linked by 4° wedge-shaped tracks. The stability of the SBDSS surface was evaluated under continuous sunlight exposure from January 7 to 13, 2026, in Qinhuangdao, China. Relevant environmental parameters were recorded in Table S3. The experimental results (Fig. S11) showed that after 7 days of sunlight exposure, the surface wettability did not change significantly, and the performance remained stable. It is worth noting that sunlight contains both ultraviolet and infrared rays. Ultraviolet rays can lead to competitive adsorption of water, while infrared rays heat the surface, thereby promoting competitive adsorption of oxygen. The competitive adsorption of oxygen and water on the surface achieves a dynamic equilibrium, maintaining stable wettability. This is consistent with our previous findings on the light-controlled wettability of TiO_2[14,31]. Subsequent sandpaper abrasion (Fig. S12) and water impact (Fig. S13) tests further confirmed that the surface could maintain its superhydrophobic properties under mechanical wear and fluid impact, demonstrating good adhesion strength and environmental tolerance. Then, to better understand the fog collection mechanism of this structure, further experiments were conducted.

Efficient Fog Collection of the SBDSS

To study the optimal size and wettability of SBDSS for fog capture, experiments were conducted using a laboratory device to assess fog collection efficiency (Fig. 4a).

The SBDSS is specifically designed for water collection, with a main trunk and side branches. The schematic

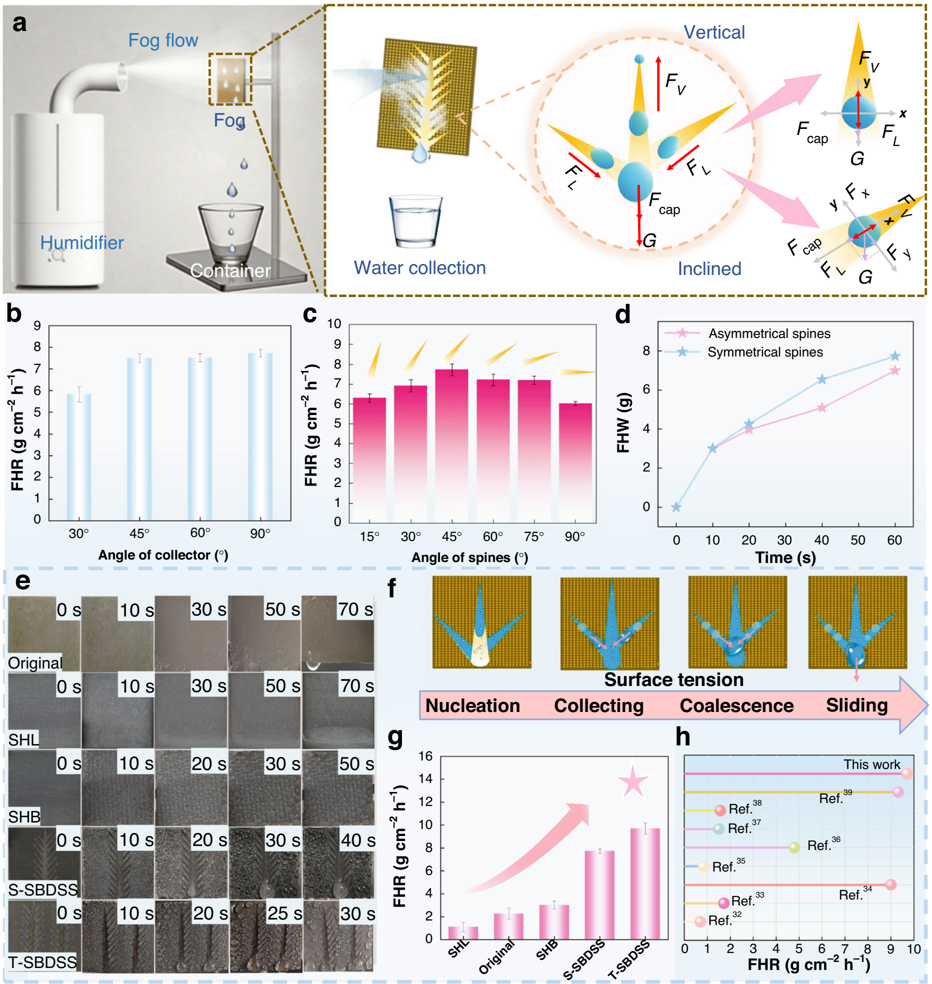

Fig. 4 Optimisation and benchmarking of the SBDSS. **a** Test setup and droplet force balance. **b** FHR as a function of collector tilt. **c** Fog-harvesting rate (FHR) versus spine angle. **d** Cumulative fog-harvesting weight (FHW) for symmetric (blue) and asymmetric (pink) spines. **e** Time-lapse microscopy (0–70 s) of original Ti, super-hydrophilic (SHL), super-hydrophobic (SHB), single- structure SBDSS (S-SBDSS) and two-structure SBDSS (T-SBDSS). **f** Four-stage droplet evolution on SBDSS: nucleation, guided collection, coalescence and low-hysteresis sliding. **g** water captured by differently treated samples within 1 hour, including original samples, SHL, SHB, S-SBDSS, T-SBDSS. **h** Comparison of the FHR in this work and other published research

illustrates the transient mass transfer of a fog droplet at the junction between the dendritic trunk and its lateral branches. As fog droplets encounter the structure, incoming airflow drag captures them onto the super-hydrophilic side branches. Upon contact, the droplets immediately spread across the surface and are pinned at the contact line, preventing any rebound. A wettability gradient, ranging from hydrophilic to super-hydrophilic, is strategically incorporated along the tapering trunk. Combined with the Laplace pressure difference created by the conical geometry, this gradient generates a unidirectional capillary force. This force pulls the liquid from the branches into the trunk and directs it downward. As droplets grow, coalescence increases the curvature radius, lowering the Laplace pressure locally, while the high curvature at the narrow end of the trunk maintains the continuous driving force. As the droplet expands, its increasing size amplifies the gravitational component of the interfacial traction, thus accelerating the drainage process. The inclination of the trunk and branches resolves the gravitational force into a downslope component, which works in synergy with the capillary gradient, facilitating rapid, unidirectional liquid transport without causing clogging. The wedge-profile design of both the trunk and the branches generate additional Laplace pressure, effectively driving condensed droplets from the tip toward the base. This geometry, combined with the sequential stages of fog collection—condensation, growth, coalescence, and surface drainage—ensures high efficiency in water harvesting. Initially, droplets nucleate on the micro/nanostructured hydrophilic side branches. Capillary action, driven by the Laplace pressure, moves the droplets toward the main trunk, where they coalesce into larger volumes. This continuous growth process is sustained by the synergistic effects of capillary action, Laplace pressure, and surface tension. The gravitational component further aids in the downward movement, promoting droplet merging during transit.

To maximize water collection efficiency, structural parameters are optimized through experimental analysis. As shown in (Fig. 4b), the collector maintains effective fog capture across all placement angles (β), demonstrating operational adaptability. The FHR increases with β, peaking at 90°. At 90°, the fog collection rate of SBDSS reaches $7.72\,\mathrm{g{\cdot}cm^{-2}{\cdot}h^{-1}}$, a 61.62% improvement over the 15° rate ($10.142\,\mathrm{mg{\cdot}cm^{-2}{\cdot}h^{-1}}$). Additionally, FHR measurements at varying side-branch angles (θ) reveal a non-monotonic trend. Minimal gravitational components cause inadequate drainage force. Prolonged surface residence promotes droplet aggregation without effective coalescence. Resultant droplets adhere strongly due to surface tension, inhibiting sliding and reducing FHR. However, Excessive gravitational acceleration causes premature droplet sliding. Insufficient residence time limits coalescence opportunities, diminishing collection effectiveness. Maximum FHR occurs at $\theta = 45°$ (Fig. 4c), where equilibrium between gravitational drive, surface tension, and capillary action optimizes coalescence time, gravity-assisted sliding, and continuous drainage without adhesion, improving fog collection. Furthermore, FHR variations are examined for symmetric and asymmetric side-branch structures (Fig. 4d). In hydrophilic regions, symmetric branches allow droplets to reach critical size before gravitational removal. Asymmetric designs mitigate localized droplet accumulation while promoting coalescence, forming larger droplets that slide rapidly under gravity. This structural configuration ensures continuous fog supply, increases droplet-collector contact area, and enhances collection efficiency. High-speed imaging captures dynamic capture-growth-shedding processes on original titanium, super-hydrophilic (SHL), super-hydrophobic (SHB), single- structure SBDSS (S-SBDSS) and two-structure SBDSS (T-SBDSS) (Fig. 4e and Fig. S14). SBDSS with a mixed-wettability surface featuring dual structures demonstrates optimal water collection performance. Performance enhancement arises from synergistic interfacial and gravitational dynamics. Superhydrophilic regions promote rapid droplet spreading, reducing contact angles and minimizing surface energy barriers, while hydrophobic domains facilitate directional transport through interfacial tension gradients. This combination enables efficient droplet nucleation, growth, and spontaneous directional movement, significantly boosting overall water harvesting efficiency. Concurrently, gravity-driven directional transport propels droplets toward the trunk terminus via optimized branch inclination. Crucially, the structure prevents large-droplet accumulation through Laplace pressure gradients engineered within tapered microchannels, while continuous heterogeneous nucleation on vertical surfaces sustains droplet renewal cycles. These mechanisms maximize liquid throughput by balancing removal of mature droplets with generation of microdroplets across the active surface area. Fig. 4f illustrates the dynamic fog collection process across four distinct stages: nucleation, collecting, coalescence, and sliding. The combined effects of wettability and structural gradients work synergistically to enhance droplet generation rates and increase the mass of individual droplets. In the nucleation phase, droplets begin to form at the edges of the side branches. These initial droplets, with diameters on the order of hundreds of micrometers, are generated due to the hydrophilic nature of the surface. During the collecting phase, these droplets migrate toward the main trunk, driven by the wettability and structural gradients that facilitate movement. As the droplets approach the trunk, dual menisci form at the interface between the droplet and the surface. The resulting Laplace pressure begins to fill the spine tip first, progressively saturating the trunk as the droplets grow.

In the coalescence phase, droplets continue to merge, increasing in size as additional droplets converge. This merging process further enhances the Laplace pressure and capillary forces, propelling the droplets toward the base of the trunk. Finally, in the sliding phase, droplet detachment occurs when the gravitational force (G) exceeds the capillary retention force. At this point, the droplet slides down the trunk, completing the collection process. Table S2 and Fig. S15 illustrates the mechanism of S-SBDSS for fog harvesting enhancement. Results confirm lowest efficiency on fully hydrophilic surfaces (liquid film inhibits coalescence), while T-SBDSS delivers peak performance ($9.7\,\mathrm{g{\cdot}cm^{-2}{\cdot}h^{-1}}$) (Fig. 4g). Comparative analysis confirms the superior performance among bioinspired asymmetric-wetting fog harvesters (Fig. 4h)[32–39]. Through the evaluation of the durability, stability, and water collection cycle of this structure, Fig. S16 and Fig. S17 further highlight the exceptional durability of the T-SBDSS structure, demonstrating stable performance over multiple cycles even after 20 days. The results show that the water collection weight remains consistently high, which indicates that the structure possesses high efficiency and sustainability. This finding confirms that the structure is capable for collecting water effectively over the long term, thereby providing a stable and reliable water source for the system.

System Performance Evaluation of D-TENG

In conventional water harvesters, the substantial kinetic energy of droplet impact on the collector is directly

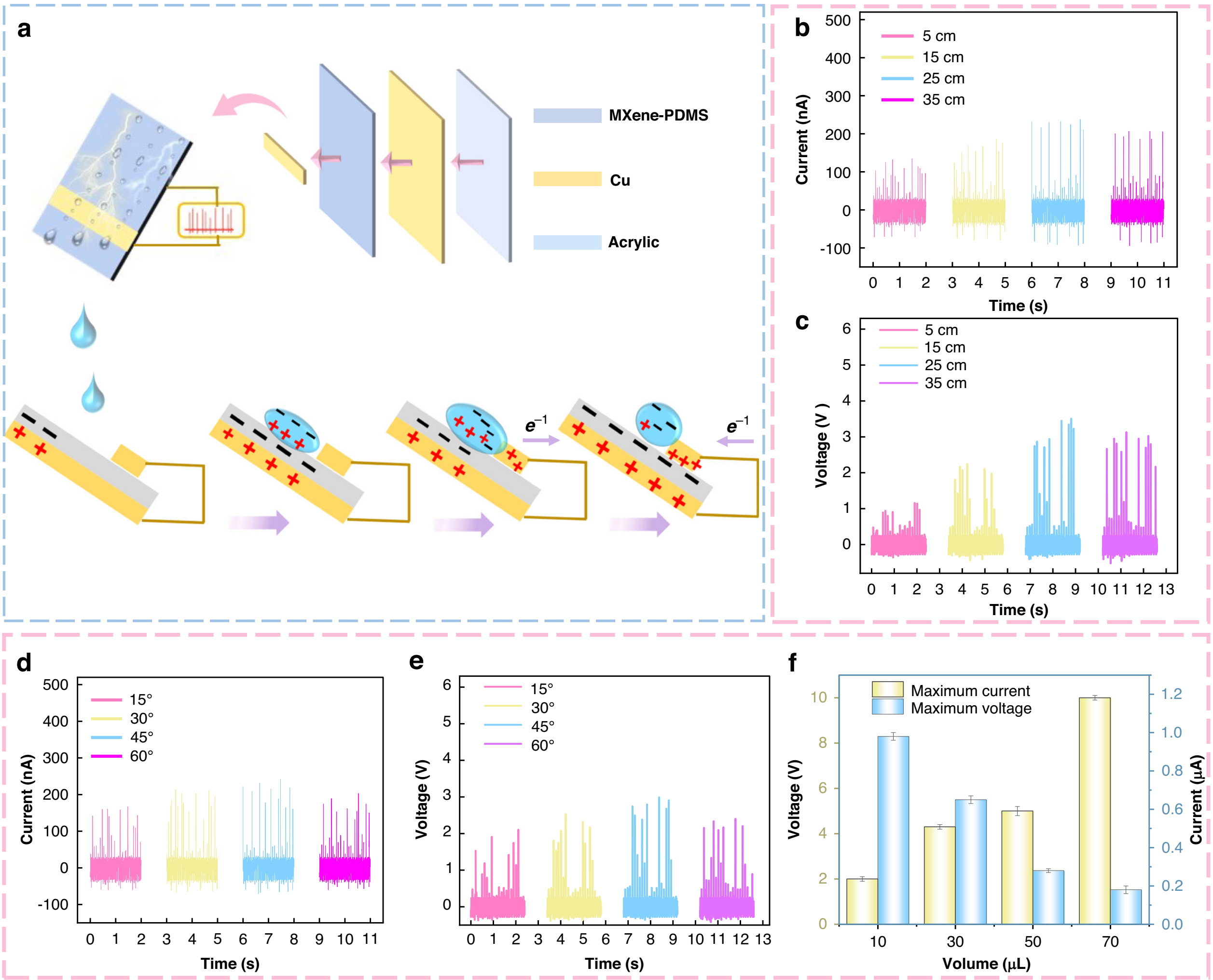

Fig. 5 Output performance of the D-TENG. a Schematic and Working mechanism of the D-TENG. **b**, **c** Output current and voltage generated by the D-TENG when droplets are released from different heights of the triboelectric layer. **d**, **e** Output current and voltage generated by the D-TENG when droplets are released from different tilt angle of the triboelectric layer. **f** Output current and voltage generated from different droplet volumes, all values are reported based on single-impact transient testing

dissipated, ignoring effectively harvesting electrostatic energy from the liquid-solid interface[40,41]. Herein, droplet-driven triboelectric nanogenerator(D-TENG) offer a promising solution for harvesting energy from low-frequency, low driving force, and high-entropy droplet sources. As is shown in Fig. 5a, the operational mechanism D-TENG from the liquid-solid interface. there is no electrode charge transfer occurring before droplet contact, impact-induced droplet spreading triggers immediate downward charge transfer between the dielectric layer and the top electrode, generating electrical signals that reverse during detachment as electrons return to the upper electrode. The performance of D-TENG is primarily determined by using the dielectric layer with high charge storage capacity[42]. Furthermore, the triboelectric layer should be constructed from a highly hydrophobic material to suppress performance degradation caused by sediment shielding and surface wetting in practical environments, thereby facilitating effective droplet sliding and minimizing residual droplet retention. As a uniquely emerging material, MXene balances conductivity and triboelectric properties, though susceptible to oxidation. The oxidative stability of MXene poses a key challenge that limits its long-term reliability in practical applications. Integrating MXene with PDMS enhances mechanical robustness while preserving triboelectric functionality, yielding an optimized MXene-PDMS composite. By incorporating PDMS, the hydrophobic properties of the composite film surface are enhanced (Fig. S18). The MXene/PDMS composite serves as the electrode layer and is encapsulated by a pure PDMS overlayer, preventing exposure of the MXene surface. EDS analysis

(Fig. S19) confirms that the surface is dominated by PDMS elements (Si ≈ 41.0 wt%, C ≈ 36.3 wt%, O ≈ 22.7 wt %) with no detectable Ti (0.0 wt%), ensuring the encapsulation of MXene and preventing charge leakage, which is further supported by stable device operation (e.g., driving LEDs). As displayed in Fig. S20 at an optimal loading of 2 wt%, the composite achieves a synergistic enhancement of superhydrophobicity (WCA = 152°) and maximum charge output (Fig. S21).

As shown in Fig. 5a, MXene-PDMS serves as dielectric layer, copper foil with 500 μm-thick acts as both the top and bottom electrodes, while an acrylic plate is used as the substrate. The droplet volume is fixed at 30 ± 0.2 μL with deposition intervals of 2 ± 0.5 s. Under a fixed droplet volume, this study systematically investigated the influence of release height (10–35 cm) on the electrical output performance of the D-TENG. The results indicate that both peak voltage and current first increased, reached a maximum at 25 cm (3.5 V, 0.25 μA), and then decreased with increasing height (Fig. 5b, c). This is attributed to the height-regulated kinetic energy of the droplet impact: moderate heights enhance contact area and charge separation rate, improving charge transfer efficiency; whereas excessive heights induce droplet splashing and surface residue, leading to charge leakage and shielding effects that degrade output performance. We further study the tilt angle optimization (15.0°–60.0°) of the D-TENG, which shows peak voltage and current maximum (3.1 V, 0.22 μA) at a 45°tilt angle, representing a 156% and 137% increase compared to the 15° (Fig. 5d, e). Mechanistic analysis reveals that moderate tilting 45° synergistically optimizes droplet contact area and detachment speed, achieving an optimal balance between sufficient charge transfer and efficient charge separation (Video S1). In contrast, nearly horizontal surface suffers from charge leakage due to residual liquid film, while approaching the vertical surface limits charge transfer due to insufficient contact time—both suppressing output performance. These results all indicate that the contact area between the droplet and the dielectric layer significantly influences the output performance, as the electrostatic induction area increases, the output charge and voltage will be enhanced. Under fixed conditions of falling height (20 cm), ambient temperature and humidity (25 °C, 75% ± 5% RH), and load resistance (100 MΩ), the influence of droplet volume (10–70 μL) on the electrical output performance of the D-TENG was systematically investigated. As shown in Fig. 5f, the peak voltage decreases monotonically with increasing droplet volume, dropping from 10 V at 10 μL to 2 V at 70 μL, while the peak current increases significantly from 0.18 μA to 0.98 μA. This opposite regulatory trend arises from the volume-dependent charge transfer mechanism at the droplet-triboelectric layer interface. Smaller droplets, with their smaller contact area, higher charge density, and rapid detachment, facilitate higher voltage output. In contrast, although larger droplets exhibit reduced charge density, the total transferred charge increases with the expanded contact area, driving a stronger current. At 30 μL, the device achieves an optimal balance between voltage and current, with the average output power reaching its peak (~ 2.79 μW), providing a volume optimization window for practical droplet energy harvesting applications. These results establish that D-TENG efficiency depends critically on dielectric layer properties and operational parameters, with MXene-PDMS composite demonstrating superior triboelectric performance through synergistic enhancement of mechanical stability, charge transfer efficiency, and droplet energy harvesting performance. The durability of the MXene–PDMS composite was evaluated under three relevant outdoor stressors: mechanical wear (1200 abrasion cycles), hydraulic erosion (180 min droplet impact), and light aging (7 days of light exposure). The detailed results are shown in Fig. S22, confirming its reliability and stability as a dielectric layer.

Therefore, combining the efficient fog collection capability of NBIS with the power generation capacity of D-TENG can further enhance the overall energy utilization efficiency of the system, offering new possibilities for green energy and resource utilization. Given the pulsed, low-power nature of droplet-driven outputs, the harvested electricity is most practically used via rectification and energy storage to support intermittent off-grid functions (e.g., duty-cycled sensing, event-triggered indicators/alarms, and low-duty wireless transmission), rather than continuous powering of high-power loads[43,44].

Demonstration of the NBIS Applications

To verify electricity generation from fog, a water collection and power generation unit was assembled on the NBIS, with a humidifier used to simulate different fog flows (Fig. 6a). Experiments mimic the natural atmospheric moisture cycle under controlled conditions (24 ± 0.5 °C, 75 ± 1.0% RH;) to evaluate fog harvesting performance (Fig. S23). The 3D-printed cylindrical mesh chamber mold (20 ± 0.1 cm diameter) integrates 25 T-SBDSS units into a FWCC, enabling directional droplet capture while simultaneously facilitating adsorption and liquid transport. Atmospheric fog condenses on patterned T-SBDSS of FWCC, with nucleation occurring on side branches followed by coalescence along tapered collection channels. Droplets initially nucleate on side branches, then coalesce along the wedge-shaped main groove. Upon reaching a critical volume, collected water droplets are driven by gravity to the collection unit. The harvested water is stored in the FWCC. Once it reaches a height of 2.5 cm, the water is channeled through a drip tube to

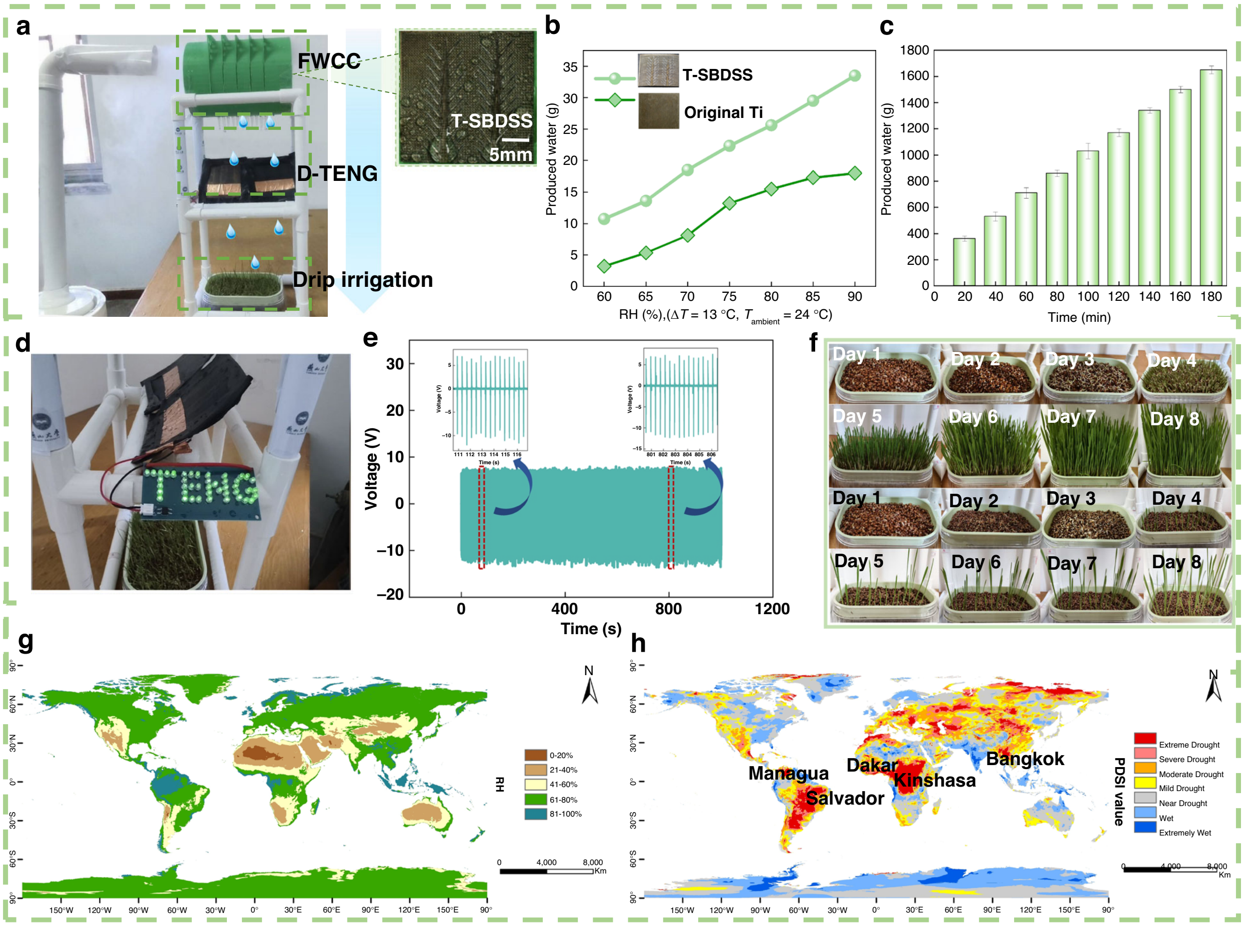

Fig. 6 Application of NBIS based on fog harvesting and energy production. a Schematic overview of the system for fog collection and energy supply under laboratory conditions. **b** Comparison of water collection rates between T-SBDSS and original titanium after adding RH. **c** yields water during 3.0 ± 0.2 h dense fog through NBIS. **d** Image of light-emitting diodes (LEDs) powered by NBIS. **e** Short-voltage for 100 cycles of the D-TENG. **f** Images of plant growth are shown over eight consecutive days, demonstrating the impact of NBIS on plant development. **g** Geographical representation of global soil moisture conditions from 2019-2024 (adapted from ERA5). The data indicates regions of extreme drought to extremely wet conditions, highlighting the variation across different continents. **h** Inset maps showing moisture index distribution for specific regions: Mangua (Ecuador), Salvador (San Salvador), Dakar (Senegal), Kinshasa (DRC), and Bangkok (Thailand)

impact the D-TENG surface, enabling droplet-based power generation. Flowing along the 45.0°-inclined D-TENG surface fabricated with a 25.0 cm^2 MXene-PDMS active layer, the droplets activate the device (Video S2), generating a triboelectric output via sequential contact–separation events between the droplet and the interdigitated electrodes. As illustrated in Fig. 6b, the T-SBDSS exhibits remarkable humidity adaptability, showing a water collection rate at > 80% RH approximately 3.2 times greater than that at 60% RH, significantly outperforming pristine titanium. Further system evaluation (Fig. 6c) demonstrates that a module with an active area of 0.350 ± 0.005 m^2 produces 1600 ± 50 mL of water over 10 h of nocturnal operation under simulated fog flow conditions, fulfilling ≈83% of the daily drinking water requirement (1.93 L) for an individual in arid regions. Although the current NBIS lacks an integrated filtration unit, its outlet is designed for modular connection to downstream purification systems. Extensive experience with relevant separation technologies has been demonstrated in our prior work. Established wettability-based separation methods support this compatibility. Examples include practical separation/filtration configurations based on switchable-wettability graphene composite coatings with documented chemical stability[14] and anti-fouling switchable-wettability surfaces for controllable oil–water separation[45], as well as bioinspired interlaced-wetting interfaces for continuous on-demand emulsion separation[46,47]. Based on this expertise, a modular post-treatment cartridge can be readily integrated in future iterations. This cartridge may utilize mesh or nonwoven membranes for particulate prefiltration, followed by adsorption or disinfection processes tailored to specific water quality objectives. This modification will not disrupt the fog-collection mechanism. Final water quality characterization and compliance testing remain necessary before use for agricultural or drinking purposes. The water collection rate increases with ΔT and RH (Fig. S24,a-b), with T-SBDSS outperforming Ti, and a dew-point map (Fig. S24,c) estimates condensation feasibility based on local T ambient and RH, while wind effects are qualitatively discussed. Fig. S25 shows the detailed configuration of the integrated system, where water is directed through gravity-fed drip streams into the D-TENG impact zones. Sealed drainage paths prevent leakage and electrical short circuits, while the PVC frame provides structural support and electrical isolation, ensuring reliable operation in environment. Owing to its easy integrability, the D-TENG also demonstrates excellent scalability. The parallel connection of multiple units enhances current output (Fig. S26), enabling the direct powering of an LED during operation (Fig. 6d and Video S3). LED lighting serves as a proof-of-concept, mimicking photosynthesis-related illumination in off-grid agro-environments. In off-grid applications, the D-TENG powers low-voltage systems for sensing and monitoring, using rectification and small energy storage. A comparative analysis is provided in Table S4. Electrically, the D-TENG readily achieves an open-circuit voltage (Voc) exceeding 5 V. Moreover, the D-TENG demonstrates outstanding mechanical durability, maintaining a stable output voltage of 5 V over 1000 operational cycles (Fig. 6e). The superhydrophobic D-TENG surface prevents droplet accumulation, which maximizes contact separation efficiency and ensures continuous power generation under steady droplet flow, thus supporting the long-term operation of small electronics (Fig. S27). In the cyclic tests conducted after over 300 days, the surface maintained good stability (Fig. S28). However, copper is still prone to oxidation in humid environments. To ensure longer-lasting performance and enhance durability, the Cu electrodes can be placed underneath the MXene–PDMS dielectric and the edges/lead exits can be sealed to prevent water contact with the metal, thereby reducing corrosion.

In off-grid agricultural environments, where access to conventional power is limited, D-TENG-based energy harvesting systems provide a sustainable solution. As shown in Fig. S29, multiple D-TENG units harvest energy from ambient water droplets, which is rectified and stored in a capacitor. This energy powers low-energy agricultural applications, including wireless sensors, event-triggered indicators, and electric fences. By combining energy harvesting with storage, the system ensures stable power for intermittent tasks like monitoring soil moisture, triggering alerts, and protecting crops, offering a scalable solution for rural and remote areas. The NBIS also displays significant potential in agricultural applications. As depicted in Fig. 6f, barley seeds sown in a blank growth matrix and irrigated daily with fog water collected by the system showed initial germination within 48 h, reaching near-complete germination by the third day. By day seven, seedlings irrigated with NBIS-harvested water exhibited markedly enhanced growth velocity and plant height compared to the non-irrigated control group. To contextualize the electrical output within integrated water–energy harvesters, reported performance metrics of representative systems are compiled in Table S5, and a normalized (1–5) radar chart benchmark is provided in Fig. S30, highlighting the advance of a robust, agriculturally relevant fog-water–electricity co-supply module. Considering that the system exhibits pronounced humidity tolerance, alongside global analyses which indicate persistent drought in high-humidity regions due to seasonal rainfall deficits and elevated evaporation (Fig. 6g). Crucially, the NBIS operational flexibility is designed to address this very heterogeneity. The considerable application potential of the NBIS is demonstrated for some locations. Notably, in Salvador, Bangkok, where relative humidity is high ($RH_{avg} \approx 96.4\%$) and extreme drought, the water production capacity can reach up to 4.6 L/m^2 per day. In normal mode, the system is applicable to most regions worldwide (Fig. 6h). The viability of the system across diverse climates, from arid to humid, strongly demonstrates its potential for decentralized water harvesting and agricultural irrigation on a global scale.

Conclusion

In this study, we present a novel bioinspired integrated system (NBIS) that combines synergistic biomimetic dendritic structured surface (SBDSS) with a droplet-based triboelectric nanogenerator (D-TENG) to simultaneously harvest water and generate energy. The two-structure SBDSS (T-SBDSS) achieves a fog harvesting rate of $9.7\ g{\cdot}cm^{-2}{\cdot}h^{-1}$, which is 4.3 times higher than that of untreated titanium, owing to its interlaced wetting pattern and wettability gradients. The NBIS realizes effective fog capture and spontaneous transport, while the D-TENG delivers 5.0 V output from harvested droplets. A single unit produces 1600 mL of water nightly, sufficient for basic human needs in arid regions, and successfully irrigates barley seedlings with high germination. This system significantly reduces dependence on external energy sources, overcoming the limitations of conventional methods that struggle to integrate efficient water collection and energy generation. By unlocking the dual potential of fog as a combined water and energy resource, the NBIS offers a scalable, climate-resilient solution for decentralized water–energy co-supply in water-stressed regions. Its demonstrated effectiveness at the module scale paves the way for broader application in off-grid agricultural settings.

Experimental Section

Materials

Titanium sheets (99.99% purity) and copper foils were obtained from Anhui Zhengying Metal Materials Co., Ltd. (Hefei, China), with a thickness of 0.5 mm. Chemical reagents, including polydimethylsiloxane (PDMS), curing agents, monolayer MXene dispersion (Ti_3AlC_2), and anhydrous ethanol, were purchased from Aladdin Biochemical Technology Co., Ltd. (Shanghai, China).

Fabrication of the synergistic biomimetic dendritic structured surface (SBDSS)

Titanium sheets (20 mm × 20 mm × 0.55 mm) were cleaned using an ultrasonic cleaner in ethanol for 15 min, followed by rinsing with deionized water. A circular array was designed using ezCAD software to fabricate micro/nano structures. Laser ablation was performed with a power of 20 W, a scanning speed of 1000 mm/s, and 10–40 passes. To create anisotropic wetting patterns, a dendritic structure was patterned using a laser with a power of 20–35 W and a scanning speed of 1000 mm/s, with 15–50 passes. The processed surface was then heated at 150 °C for 160 min. UV irradiation was performed on the thermally treated patterned surface using a UVA lamp (250 nm) at a power density of 2 mW/cm², with a sample-to-lamp distance of 10 cm. The wettability gradient was induced by the combined thermal and UV exposure cycles, yielding a patterned SBDSS with multilayer structures, including groove (50–400 μm) and twisted circular pit structures (diameter = 300 μm, height = 50–100 μm), as well as nanoparticles (50–200 nm).

Fabrication of the droplet-based triboelectric nanogenerator (D-TENG)

PDMS solution and monolayer MXene were mixed in a predefined mass ratio. After stirring for 5 min, the mixture was poured into a mold, degassed under vacuum for 30 min, and cured at 80 °C for 4 h. To prevent wear under natural conditions, a layer of PDMS was encapsulated on the MXene-PDMS composite. D-TENG devices were assembled using an acrylic substrate, copper foils as electrodes, and a MXene-PDMS membrane as the triboelectric layer.

Fog Collection Measurements

A custom-built indoor fog collection testing system was used to evaluate the fog collection performance of bioinspired integrated system (NBIS). A sample holder secured the sample vertically, and a commercial humidifier (BST-J20, Oudim, China) was used to generate fog with a flow rate of 50–60 cm/s. The fog droplet diameter ranged from 1–5 μm, and the relative humidity was maintained at 80 ± 5%, with a temperature of 24 ± 2 °C. The mass of collected water was measured using an analytical balance (FB224, Shanghai Shunyu Hengping Co., Ltd.). The fog collection rate (FHR) was calculated using the formula: (6) $\mathrm{FHR} = \boldsymbol{M} \div (\boldsymbol{A} \times \triangle \boldsymbol{T})$, where M is the mass of collected water (g), A is the surface area of the fog collector (cm²), and ΔT is the duration of the fog collection experiment (h).

D-TENG Output Performance Testing

Electrical performance of the D-TENG was evaluated in a temperature- and humidity-controlled chamber (25 °C, 75% relative humidity). The water source was positioned at a fixed height above the D-TENG, and droplet frequency was adjusted using a droplet speed controller. The tilt angle of the D-TENG was adjusted using a clamp. Open-circuit voltage and short-circuit current were measured using an electrostatic meter (Keithley 6514, Tektronix) and an oscilloscope (Keithley DMM6500, Tektronix).

Structure Characterization

The surface morphology and microstructure were characterized using scanning electron microscopy (SEM, Hitachi-3400N). The X-ray energy dispersive spectrometer (EDS, JSM-56000LV, Japan Electron Optics Laboratory Co., Ltd.) was used to observe the sample surfaces. Quantitative analysis of the elements on the surfaces of the SBDSS was performed using an X-ray photoelectron spectrometer (XPS, ESCALAB 250Xi, Thermo Fisher Scientific). The average static water contact angle (WCA) was measured at room temperature using a digital optical contact angle meter (JC-2000C1, BIOLIN, Shanghai, China). The fog collection process was recorded using a high-speed digital camera (dimax S1, PCO, Germany).

Acknowledgements

This work was supported by the National Natural Science Foundation of China (Nos. 52575347, 52205318, and U22A20183), the International Research Programs and Strategic Innovative Programs of National Key R&D Program of China (2024YFE0105500), the S&T Program of Hebei (No. 226Z3601G), the Natural Science Foundation of Hebei Province (No. E2025203083), the Science Research Project of Hebei Education Department (No. BJ2025064), and the Opening Project of the Key Laboratory of Bionic Engineering (Ministry of Education), Jilin University (K202408).

Author details

[1]Hebei Key Laboratory of Measurement Technology and Instrumentation, School of Electrical Engineering, Yanshan University, Qinhuangdao, P. R. China. [2]IN + - Center for Innovation, Technology and Policy Research, Instituto Superior Técnico, Universidade de Lisboa, Av. Rovisco Pais, Lisboa, Portugal. [3]School of Mechanical Engineering, Yancheng Institute of Technology, Yancheng, P. R. China. [4]Key Laboratory of Bionic Engineering (Ministry of Education), Jilin University, Changchun, P. R. China. [5]Institute of Structured and Architected Materials, Liaoning Academy of Materials, Shenyang, China

Data availability

The data supporting this article have been included as part of the Supplementary Information.

Competing interests

The authors declare no competing interests.

Supplementary information The online version contains supplementary material available at https://doi.org/10.1038/s41378-026-01240-1.

Received: 3 November 2025 Revised: 30 January 2026 Accepted: 26 February 2026

References

1. Bosson, J. B. et al. Future emergence of new ecosystems caused by glacial retreat. *Nature* **620**, 562–569 (2023).
2. Laleh, S. S., Safarpour, A., Shahrak, A. S., Alavi, S. H. F. & Soltani, S. Thermodynamic and exergoeconomic analyses of a novel biomass-fired combined cycle with solar energy and hydrogen and freshwater production in sports arenas. *Int. J. Hydrogen Energy* **59**, 1507–1517 (2024).
3. Rothig, T. et al. Human-induced salinity changes impact marine organisms and ecosystems. *GCB* **29**, 4731–4749 (2023).
4. He, C. et al. Future global urban water scarcity and potential solutions. *Nat. Commun.* **12**, 4667 (2021).
5. Ding, L. et al. Effective ion sieving with Ti3C2Tx MXene membranes for production of drinking water from seawater. *Nat. Sustainability* **3**, 296–302 (2020).
6. Stein, S. et al. Saline Groundwater from Coastal Aquifers As a Source for Desalination. *Environ. Sci. Technol.* **50**, 1955–1963 (2016).
7. Deng, K. M. et al. Porous structure with stable superhydrophobic surface for high-performance atmospheric fog harvesting. *J. Environ. Chem. Eng.* **10**, 108771 (2022).
8. Yu, Z. H. et al. Fog Harvesting Devices Inspired from Single to Multiple Creatures: Current Progress and Future Perspective. *Adv. Funct. Mater.* **32**, 2200359 (2022).
9. Peng, Y. et al. Magnetically Induced Fog Harvesting via Flexible Conical Arrays. *Adv. Funct. Mater.* **25**, 5967–5971 (2015).
10. Ge, C. et al. Cactus-inspired moisture harvesting for sustainable and efficient high salinity desalination. *Desalination* **583**, 117738 (2024).
11. Yu, Z. et al. Bio-inspired Copper Kirigami Motifs Leading to a 2D–3D Switchable Structure for Programmable Fog Harvesting and Water Retention. *Adv. Funct. Mater.* **33**, 2210730 (2022).
12. Zhang, P. et al. Biomimetic Superhydrophobic Triboelectric Surface Prepared by Interfacial Self-Assembly for Water Harvesting. *Adv. Funct. Mater.* **35**, 2413201 (2024).
13. Gao, H. et al. Biomimetic metal surfaces inspired by lotus and reed leaves for manipulation of microdroplets or fluids. *Appl. Surf. Sci.* **519**, 146052 (2020).
14. Gao, H. P. et al. A multifunctional graphene composite coating with switchable wettability. *Chem. Eng. J.* **415**, 128862 (2021).
15. Liu, W. et al. Micro-Droplets Parameters Monitoring in a Microfluidic Chip via Liquid-Solid Triboelectric Nanogenerator. *Adv. Mater.* **35**, 2307184 (2023).
16. Zhang, J., Lin, S., Zheng, M. & Wang, Z. L. Triboelectric Nanogenerator as a Probe for Measuring the Charge Transfer between Liquid and Solid Surfaces. *ACS Nano* **15**, 14830–14837 (2021).
17. Zhang, M. Y. et al. A droplet-based triboelectric-piezoelectric hybridized nanogenerator for scavenging mechanical energy. *Nano Energy* **104**, 107992 (2022).
18. Meng, J. et al. A New Single-Electrode Generator for Water Droplet Energy Harvesting with A 3 mA Current Output. *Adv. Energy Mater.* **14**, 2303298 (2023).
19. Wang, W. et al. High-Output Single-Electrode Droplet Triboelectric Nanogenerator Based on Asymmetrical Distribution Electrostatic Induction Enhancement. *Small* **19**, e2301568 (2023).
20. Huang, X. et al. Droplet-Based Electricity Generator toward Practicality: Configuration, Optimization, and Hybrid Integration. *Adv. Mater. Technol.* **8**, 2201369 (2022).
21. Qu, H., Wan, L., Tian, Z., Liu, G. & Wang, Z. L. Evaporation Triboelectric-Nanogenerator: Harvesting Low-Grade Heat Energy from Ambient Environment. *Adv. Mater. Technol.* **9**, 2301409 (2023).
22. Wei, X. et al. All-Weather Droplet-Based Triboelectric Nanogenerator for Wave Energy Harvesting. *ACS Nano* **15**, 13200–13208 (2021).
23. Hou, Z. et al. UV-emitting upconversion-based TiO2 photosensitizing nanoplatform: near-infrared light mediated in vivo photodynamic therapy via mitochondria-involved apoptosis pathway. *ACS Nano* **9**, 2584–2599 (2015).
24. Ouyang, W. X., Teng, F. & Fang, X. S. High Performance BiOCl Nanosheets/TiO Nanotube Arrays Heterojunction UV Photodetector: The Influences of Self-Induced Inner Electric Fields in the BiOCl Nanosheets. *Adv. Funct. Mater.* **28**, 1707178 (2018).
25. Wang, L. et al. Dual-Energy-Barrier Stable Superhydrophobic Structures for Long Icing Delay. *ACS Nano* **18**, 12489–12502 (2024).
26. Wang, L. et al. Spontaneous dewetting transitions of droplets during icing & melting cycle. *Nat. Commun.* **13**, 378 (2022).
27. Liu, M., Yao, Y., Li, J., Peng, Z. & Chen, S. Directional Sliding Behavior of a Water Droplet on a Wedge-Shape Patterned Functional Surface. *J. Phys. Chem. B* **124**, 6905–6912 (2020).
28. Zhou, P., Yan, Y., Cheng, J. & Zhou, C. Directional Self-Transportation of Droplets on Superwetting Wedge-Shaped Surface in Air and Underliquid Environments. *ACS Appl. Mater. Interfaces* **15**, 8742–8750 (2023).
29. Hao, S. et al. Wetting-State-Induced Turning of Water Droplet Moving Direction on the Surface. *ACS Nano* **17**, 2182–2189 (2023).
30. Chen, H. et al. Continuous directional water transport on the peristome surface of Nepenthes alata. *Nature* **532**, 85–89 (2016).
31. Gao, H. et al. Interlaced wetting surfaces with switchable wettability for manipulating underwater oil droplets. *Chem. Eng. J.* **437**, 135007 (2022).
32. Li, C. X. et al. A Janus fibrous membrane with asymmetric wettability and surface potential for dual enhanced fog collection from the atmosphere. *Sep. Purif. Technol.* **361**, 131378 (2025).
33. Qi, X. et al. Water Collection and Transport on Bioinspired Surface Integrating Beetles, Spider Webs, and Cactus Spines. *Langmuir* **41**, 6174–6185 (2025).
34. Rajabi-Abhari, A., Soltani, M., Golovin, K. & Yan, N. Nature-inspired surface for simultaneously harvesting water and triboelectric energy from ambient humidity using polymer brush coatings. *Nano Energy* **115**, 108752 (2023).
35. Wei, H. et al. Efficient fog harvesting system inspired by cactus spine and spider silk with vertical crisscross spindle structure. *Chem. Eng. J.* **507**, 160747 (2025).
36. Xiao, J., Zhang, X. & Wang, Z. Sandwiched Copper Foam with Symmetrical Wettability for Direction-Independent Fog Collection. *Langmuir* **41**, 6389–6397 (2025).
37. Zhan, D. et al. Improved Fog Collection on a Hybrid Surface with Acylated Cellulose Coating. *ACS Appl. Mater. Interfaces.* **16**, 27657–27667 (2024).
38. Zhang, C. et al. Callistemon Viminalis-Inspired Rotational Structure for Omnidirectional Fog Collection and Power Generation. *Adv. Funct. Mater.* **35**, 2505075 (2025).
39. Zhang, S. et al. Bioinspired asymmetric amphiphilic surface for triboelectric enhanced efficient water harvesting. *Nat. Commun.* **13**, 4168 (2022).
40. Luo, B. et al. Triboelectric charge-separable probes for quantificationally charge investigating at the liquid-solid interface. *Nano Energy* **113**, 108532 (2023).
41. Luo, B. et al. Liquid-Solid Triboelectric Probes for Bubbles Status Monitoring. *Adv. Funct. Mater.* **34**, 2315725 (2024).
42. Zhou, Y. et al. Universal droplet propulsion by dynamic surface-charge wetting. *Microsyst. Nanoeng.* **10**, 134 (2024).
43. Cheng, X. et al. Power management and effective energy storage of pulsed output from triboelectric nanogenerator. *Nano Energy* **61**, 517–532 (2019).
44. Dai, S., Li, X., Jiang, C., Ping, J. & Ying, Y. Triboelectric nanogenerators for smart agriculture. *InfoMat* **5**, e12391 (2023).
45. Gao, H. et al. Switchable Wettability Surface with Chemical Stability and Antifouling Properties for Controllable Oil-Water Separation. *Langmuir* **35**, 4498–4508 (2019).
46. Gao, H. et al. Bioinspired interlaced wetting surfaces for continuous on-demand emulsion separation. *J. Hazard. Mater.* **480**, 136011 (2024).
47. Gao, H. et al. A wood–electric-eel inspired biomimetic membrane with self-monitoring capability for efficient oily wastewater treatment. *J. Hazard. Mater.* **503**, 141038 (2026).